

Air pollution satellite-based CO₂ emission inversion: system evaluation, sensitivity analysis, and future research direction

Hui Li^{1,2}, Jiaxin Qiu^{1,2}, Bo Zheng^{1,2,*}

¹Shenzhen Key Laboratory of Ecological Remediation and Carbon Sequestration, Institute of Environment and Ecology, Tsinghua Shenzhen International Graduate School, Tsinghua University, Shenzhen 518055, China.

²State Environmental Protection Key Laboratory of Sources and Control of Air Pollution Complex, Beijing 100084, China.

Correspondence to: Bo Zheng (bozheng@sz.tsinghua.edu.cn)

Abstract. Simultaneous monitoring of greenhouse gases and air pollutant emissions is crucial for combating global warming and air pollution. We previously established an air pollution satellite-based carbon dioxide (CO₂) emission inversion system, successfully capturing CO₂ and nitrogen oxides (NO_x) emission fluctuations amid socioeconomic changes. However, the system's robustness and weaknesses have not yet been fully evaluated. Here, we conduct a comprehensive sensitivity analysis with 31 tests on various factors including prior, model resolution, satellite constraint, and inversion system configuration to assess the vulnerability of emission estimates across temporal, sectoral, and spatial dimensions. The Relative Change (RC) between these tests and Base inversion reflects the different configurations' impact on inferred emissions, with one standard deviation (1σ) of RC indicating consistency. Although estimates show increased sensitivity to tested factors at finer scales, the system demonstrates notable robustness, especially for annual national total NO_x and CO₂ emissions across most tests ($RC < 4.0\%$). Spatiotemporally diverse changes in parameters tend to yield inconsistent impacts ($1\sigma \geq 4\%$) on estimates, and vice versa ($1\sigma < 4\%$). The model resolution, satellite constraint, and NO_x emission factors emerge as the major influential factors, underscoring their priority for further optimization. Taking daily national total CO₂ emissions as an example, the $\overline{RC} \pm 1\sigma$ they incur can reach $-1.2 \pm 6.0\%$, $1.3 \pm 3.9\%$, and $10.7 \pm 0.7\%$, respectively. This study reveals the robustness and areas for improvement in our air pollution satellite-based CO₂ emission inversion system, offering opportunities to enhance the reliability of CO₂ emission monitoring in the future.

1 Introduction

The knowledge of emissions, i.e., how much, where, and by what activity pollutants are released into the atmosphere, lays the foundation for understanding the changes in atmospheric compositions and managing emissions toward climate and air quality targets (Meinshausen et al., 2022; Li et al., 2022; Zhang et al., 2019). Anthropogenic emissions are strongly modulated by socioeconomic events (e.g., holidays, economic recession, and recovery), therefore, it is essential to monitor emissions timely to interpret atmospheric species

34 concentrations (Shan et al., 2021; Le Quéré et al., 2021; Guevara et al., 2023). Currently, numerous nations,
35 particularly those within the Global South (i.e., China), grapple with the dual imperatives of mitigating air
36 pollution and addressing climate change challenges. To effectively navigate these intertwined challenges in
37 a harmonized and resource-efficient manner, the development of a system capable of disentangling variations
38 in emissions and their driving factors for greenhouse gases and air pollutants is indispensable (Ke et al., 2023).

39 Recently, a discernible trend is emerging towards inferring anthropogenic carbon dioxide (CO₂) emissions
40 from well-observed and co-emitted air pollutants (i.e., nitrogen dioxide, NO₂) given their co-emission
41 characteristics in time and space (Wren et al., 2023; Yang et al., 2023; Liu et al., 2020a; Reuter et al., 2019).
42 NO₂ forms rapidly after NO is emitted from sources and is also the primary nitrogen oxide detectable by most
43 satellites (Ye et al., 2016). This makes NO₂ a reliable and widely adopted proxy in nitrogen oxides (NO_x =
44 NO₂+NO) emission inversions. However, the co-emission of NO_x and CO₂ does not imply synchronized
45 trends in their emissions, as the CO₂-to-NO_x emission ratios and activity trends vary across different sectors
46 (Li and Zheng, 2024). The introduction of NO₂ in the CO₂ emission estimation presents several distinct
47 advantages. NO₂ has a short lifetime of several hours, rendering its source-contributing plumes readily
48 detectable via remote sensing techniques (Goldberg et al., 2019). This short lifespan of NO₂ facilitates mass-
49 balance approaches for estimating NO_x emissions, which rely on the assumption of a linear relationship
50 between NO₂ columns and local NO_x emissions (Cooper et al., 2017; Mun et al., 2023; Martin et al., 2003).
51 In contrast, the longevity of CO₂, spanning hundreds of years, combined with its elevated background
52 concentration reaching hundreds of parts per million (ppm), obscures the detection of local source-triggered
53 concentration enhancements (i.e., several ppm) (Nassar et al., 2017; Reuter et al., 2019). Moreover, remote
54 sensing technologies for NO₂ remain generally more mature, as indicated by the broader coverage and
55 improved signal-to-noise ratio in column concentration observation (Macdonald et al., 2023; Cooper et al.,
56 2022). Recent advancements in CO₂ satellite technology are promising, such as the Orbiting Carbon
57 Observatory-3 (OCO-3), which can generate CO₂ maps with a resolution of up to 1.6 km × 2.2 km and
58 monitor CO₂ columns at different times throughout the daytime to elucidate diurnal emission patterns (Taylor
59 et al., 2023), while its spatial coverage may not be sufficient for large-area inversions at high temporal
60 resolution. The synergistic quantification of CO₂ and NO_x emissions has gained substantial attention, not to
61 mention that it could provide valuable guidance for a joint effort to monitor and mitigate air pollutants and
62 carbon emissions concurrently (Miyazaki and Bowman, 2023).

63 We have developed an air pollution satellite sensor-based CO₂ emission inversion system, which is capable
64 of concurrently estimating the ten-day moving average of sector-specific anthropogenic NO_x and CO₂
65 emissions by integrating top-down and bottom-up methods. This integrated methodology has proven
66 effective in capturing emission fluctuations, particularly during the coronavirus disease 2019 (COVID-19)
67 pandemic (Zheng et al., 2020; Li et al., 2023). While previous sensitivity tests have suggested a certain level
68 of accuracy, the system has not yet undergone a comprehensive evaluation to thoroughly assess its robustness
69 and weaknesses, and thereby clearly imply its future developmental trajectory. To bridge this gap, we
70 undertake an extensive sensitivity analysis with 31 tests using the 2022 anthropogenic NO_x and CO₂ emission

71 estimation as a case study. This study investigates how emission outcomes respond to a variety of sensitivity
72 assessments across temporal, sectoral, and spatial dimensions. This study aims to diagnose and rank the
73 uncertainty sources, providing insights to prioritize improvements of this inversion system in the future.

74 **2 Materials and methods**

75 Our air pollution satellite sensor-based CO₂ emission inversion system has been elucidated in our previous
76 studies (Zheng et al., 2020; Li et al., 2023). In essence, this system integrates top-down and bottom-up data
77 streams to infer the ten-day moving average of anthropogenic NO_x and CO₂ emissions by sector in China
78 based on the mass-balance approach (Cooper et al., 2017). Comprising three key components, the system
79 involves the bottom-up inference of prior emissions for NO_x and CO₂ with sectoral profile, the top-down
80 estimation of total NO_x emissions constrained by satellite observation, and the integration of both sources to
81 derive satellite-constrained NO_x and CO₂ emissions by sector (Fig. S1). Each of these processes could
82 introduce uncertainties in the final emission estimates. To assess the potential uncertainties, we establish a
83 baseline (Base) for emissions computed using our conventional settings (Li et al., 2023; Zheng et al., 2020)
84 and further investigate sensitivity tests to characterize the impacts of the different configurations on final
85 estimates.

86 **2.1 Inversion methodology and Base inversion**

87 We use the Base inversion as a case to provide a detailed explanation of this inversion system. In the Base
88 inversion, we adhered to the same parameters and configurations outlined in previous studies for estimating
89 the ten-day moving average of anthropogenic NO_x and CO₂ emissions by sector in 2022 (Table 1) (Li et al.,
90 2023; Zheng et al., 2020). Succinctly, we first updated sectoral NO_x and CO₂ emissions from the Multi-
91 resolution Emission Inventory for China (MEIC) inventory (Zheng et al., 2018) through the bottom-up
92 process. This involved utilizing indicators including industrial production, thermal power generation, freight
93 turnover, and population-weighted heating degree days as proxies for changes in industry, power, transport,
94 and residential activity levels (Details seen in Text S1 and Table S1). Notably, to reconcile the resolution
95 between the prior emissions and the model, we aggregated the original MEIC emissions from a resolution of
96 0.25°×0.25° (Fig. S2) to 0.5°×0.625°. Secondly, we inferred the total anthropogenic NO_x emissions
97 constrained by TROPospheric Monitoring Instrument (TROPOMI) NO₂ retrievals (v2.4) (Van Geffen et al.,
98 2022) (Eq. 1). A critical step in this process was establishing a linear relationship between NO₂ tropospheric
99 vertical column densities (TVCDs) and anthropogenic NO_x emissions under the mass balance assumption
100 (Eq. 2) through GEOS-Chem simulation (v12.3.0, <https://geoschem.github.io/>) at a horizontal resolution of
101 0.5°×0.625°. Our analysis focused on the grids where anthropogenic emissions prevail (Liu et al., 2020b),
102 characterized by a ten-day moving average of NO₂ TVCDs exceeding 1×10¹⁵ molecules cm⁻².

$$103 \quad E_{t,i,TROPOMI,y} = (1 + \beta_{t,i} \left(\frac{\Delta\Omega}{\Omega} \right)_{t,i,anth,y}) \times E_{t,i,bottom-up,2019} \quad (1)$$

$$\beta_{t,i} = \frac{\Delta E_{t,i,bottom-up,2019}}{E_{t,i,bottom-up,2019}} \div \frac{\Omega_{t,i,-40\%emi,2019} - \Omega_{t,i,base,2019}}{\Omega_{t,i,base,2019}} \quad (2)$$

$$\left(\frac{\Delta\Omega}{\Omega}\right)_{t,i,anth,y} = \frac{\Omega_{t,i,sate,y}}{\Omega_{t,i,sate,2019}} - \frac{\Omega_{t,i,simu_fixemis,y}}{\Omega_{t,i,simu,2019}} \quad (3)$$

Where t , i , and y represent the ten-day window, model grid cell (i.e., $0.5^\circ \times 0.625^\circ$), and target year 2022, respectively. $E_{t,i,TROPOMI,y}$ is the anthropogenic total NO_x emissions constrained by TROPOMI NO₂ TVCDs. $E_{t,i,bottom-up,2019}$ is the anthropogenic NO_x emissions in 2019 from the MEIC. $\beta_{t,i}$ is a unitless factor relating the changes in NO₂ TVCDs to anthropogenic NO_x emissions (Lamsal et al., 2011). $\Delta E_{t,i,bottom-up,2019}/E_{t,i,bottom-up,2019}$ represent the implemented 40% reduction in anthropogenic NO_x emissions over China. The 40% reduction was selected after a series of sensitivity tests, which demonstrated that this perturbation level exerts a limited impact on the β estimates (Zheng et al., 2020). $\Omega_{t,i,-40\%emi,2019}$ and $\Omega_{t,i,base,2019}$ are GEOS-Chem simulated NO₂ TVCDs at the TROPOMI overpass time in 2019 with a 40% emission reduction and without any emission reduction, respectively. $(\Delta\Omega/\Omega)_{t,i,anth,y}$ refers to the relative changes in NO₂ TVCDs due to anthropogenic NO_x emission changes between 2019 and 2022. $\Omega_{t,i,sate,y}/\Omega_{t,i,sate,2019}$ indicates the relative differences in TROPOMI NO₂ TVCDs between 2019 and 2022, and $\Omega_{t,i,simu_fixemis,y}/\Omega_{t,i,simu,2019}$ represents the relative changes in NO₂ TVCDs caused by inter-annual meteorological variation, which are derived from GEOS-Chem simulations with the fixed 2019 emissions and meteorological field in target year.

Thirdly, we integrated the bottom-up and top-down data flows to yield TROPOMI-constrained sectoral NO_x emissions. Assuming that each grid's emission variability was primarily driven by its dominant source sectors (contributing over 50%), we utilized the discrepancy between the bottom-up and top-down estimates in grid cells dominated by a particular sector to derive sector-specific scaling factors, which were subsequently applied to correct the bottom-up sectoral NO_x emissions (Eq. 4). For grids without a sector contributing over 50%, we excluded them from sectoral scaling factor calculations, instead applying scaling factors derived from grids meeting this criterion. The number of these grids accounts for less than 20% of total grids, making their impact negligible. Following this adjustment, we rescaled the corrected bottom-up emissions to ensure alignment with the TROPOMI-constrained total emissions. The overall sectoral correction factors mainly range from 0.5 to 1.5 (Fig. S3).

$$\text{scalefactor}_{t,s,y} = 1 + \frac{\sum_i (E_{t,i,sate,y}^s - E_{t,i,bottom-up,y}^s)}{\sum_i E_{t,i,bottom-up,y}^s} \quad (4)$$

Where t , s , i , and y represent the ten-day window, sector, grid cell (i.e., $0.5^\circ \times 0.625^\circ$), and year 2022, respectively. $E_{t,i,sate,y}^s$ and $E_{t,i,bottom-up,y}^s$ are TROPOMI-constrained and bottom-up estimated NO_x emissions on grid cell i with dominated source sector s , respectively. The $\text{scalefactor}_{t,s,y}$ is the scaling factor used to correct the bottom-up estimated NO_x emissions from sectors in time t in year y .

Finally, we converted the sectoral NO_x emissions to corresponding CO₂ emissions with the CO₂-to-NO_x emission ratios derived from the bottom-up process (Eq. 5). The CO₂-to-NO_x emission ratios in 2022 are updated by reducing NO_x emission factors (EFs) while keeping CO₂ EFs unchanged based on 2019 MEIC.

137 The default assumption that the reduction rate halves annually is due to the limited potential for further
 138 reductions. In contrast, the CO₂ EFs are assumed to remain unchanged, as they are primarily determined by
 139 fuel type and combustion conditions (Cheng et al., 2021) (details seen in Text S2).

$$140 \quad C_{s,t,i,TROPOMI,y} = E_{s,t,i,TROPOMI,y} \times \frac{EF_{CO_2 s,i,bottom-up,2019}}{EF_{NO_x s,i,bottom-up,2019} \times (1 - rNO_{x,s,i,y})} \quad (5)$$

141 Where $C_{s,t,i,TROPOMI,y}$ and $E_{s,t,i,TROPOMI,y}$ are CO₂ and NO_x emissions from sector s . $EF_{CO_2 s,i,bottom-up,2019}$ and
 142 $EF_{NO_x s,i,bottom-up,2019}$ are the sectoral EFs of CO₂ and NO_x in 2019 derived from the MEIC emission model.
 143 $rNO_{x,s,i,y}$ is the reduction ratio in NO_x EFs by sector from 2019 to 2022 derived from the bottom-up estimation.

144 We approximate the annual NO_x and CO₂ emissions as the sum of the ten-day moving average of NO_x and
 145 CO₂ emissions in 2022 with a vacancy in the first and last five days. This approximation, however, does not
 146 impact our analysis, as our primary objective is to identify potential sources of uncertainty within the system
 147 and thereby highlight areas for future improvement.

148 **Table 1. Configurations of Base inversion.**

Factors/parameters	Base setting
GEOS-Chem (GC) resolution	GEOS-Chem simulation with the resolution of 0.5°×0.625°
TROPOMI retrievals version	v2.4 of TROPOMI NO ₂
TROPOMI screening schemes	Cloud fraction (CF)<0.4, quality flag (QA)>0.5
Reference year	2019
NO _x emission factors (EFs)	The reduction ratio of NO _x EFs halves annually*
Threshold value to identify dominant emission source sectors for each grid	50%
Sectors in bottom-up estimation	8 sectors (power, industry, cement, iron, residential, residential-bio, on-road, and off-road)

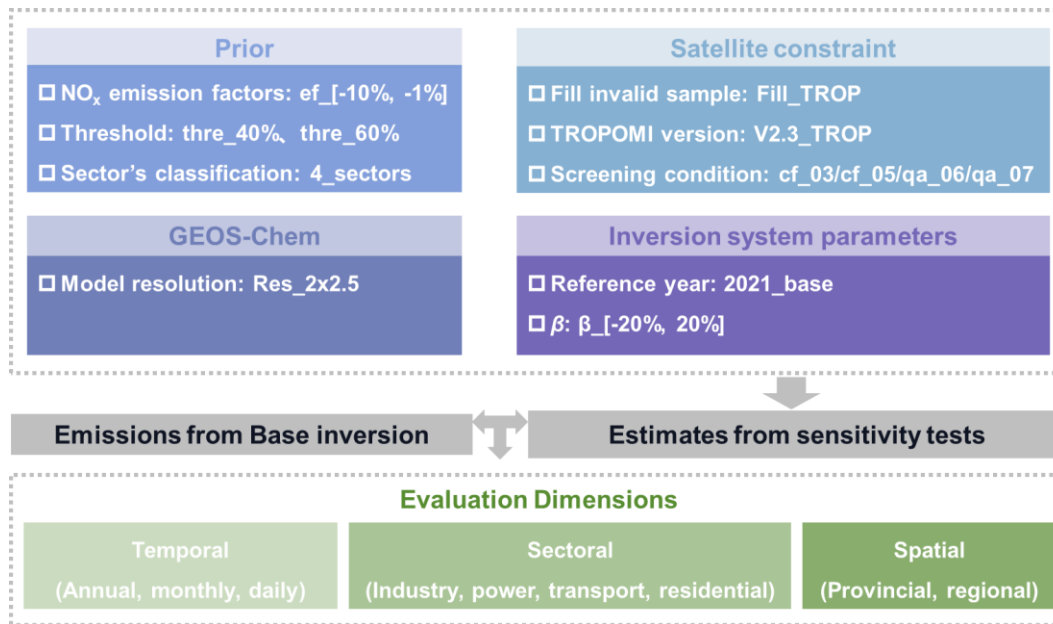
149 *Each year's reduction rate for NO_x EFs is set to decrease by half compared to the previous year. For example, if the reduction of NO_x
 150 EFs from 2019 to 2020 was 4%, the reduction from 2020 to 2021 would be set at 2%.

151 2.2 Sensitivity settings

152 The sensitivity inversion experiments comprise 31 tests designed to provide a comprehensive evaluation of
 153 the system. To facilitate a clearer discussion of their impacts, we categorized these tests into four classes
 154 based on their roles within the system: prior information, GEOS-Chem model resolution, satellite
 155 observational constraints, and inversion system parameters (Fig. 1 and Table 2). Each test is conducted as a
 156 controlled experiment, where only one parameter is altered while the rest remain the same as their Base
 157 inversion setting. The rationale behind the settings and their design will be elaborated in the following
 158 sections.

Table 2. Settings of 31 sensitivity inversion tests.

Category	Num	Name	Settings description	Test objectives
GC	1	Res_2×2.5	GEOS-Chem simulation with the resolution of 2°×2.5°	Model resolution
	2	Trop_fill	Complementing TROPOMI NO ₂ with machine learning	Sampling coverage
	3	Trop_v2.3	Substituting TROPOMI NO ₂ from v2.4 to v2.3	Satellite data version
Satellite constraint	4	Trop_cf03	Changing CF limit from 0.4 to 0.3	Satellite data filtering condition
	5	Trop_cf05	Changing CF limit from 0.4 to 0.5	
	6	Trop_qa06	Changing QA limit from 0.5 to 0.6	
	7	Trop_qa07	Changing QA limit from 0.5 to 0.7	
Inversion system parameters	8	2021_base	Changing the reference year from 2019 to 2021	Reference year
	9	β_-20%	Scaling β down by 20%	β
	10	β_-15%	Scaling β down by 15%	
	11	β_-10%	Scaling β down by 10%	
	12	β_-5%	Scaling β down by 5%	
	13	β_-1%	Scaling β down by 1%	
	14	β_1%	Scaling β up by 1%	
	15	β_5%	Scaling β up by 5%	
	16	β_10%	Scaling β up by 10%	
	17	β_15%	Scaling β up by 15%	
18	β_20%	Scaling β up by 20%		
Prior	19	ef_-10%	Scaling changes in NO _x EFs down by 10%	NO _x EFs
	20	ef_-9%	Scaling changes in NO _x EFs down by 9%	
	21	ef_-8%	Scaling changes in NO _x EFs down by 8%	
	22	ef_-7%	Scaling changes in NO _x EFs down by 7%	
	23	ef_-6%	Scaling changes in NO _x EFs down by 6%	
	24	ef_-5%	Scaling changes in NO _x EFs down by 5%	
	25	ef_-4%	Scaling changes in NO _x EFs down by 4%	
	26	ef_-3%	Scaling changes in NO _x EFs down by 3%	
	27	ef_-2%	Scaling changes in NO _x EFs down by 2%	
	28	ef_-1%	Scaling changes in NO _x EFs down by 1%	
	29	thre_40%	Changing the dominant sector threshold from 50% to 40%	Threshold
	30	thre_60%	Changing the dominant sector threshold from 50% to 60%	
	31	4_sectors	Aggregating the sectors from 8 to 4 in prior estimates	Sector's classification



161

162 **Figure 1. Overview of the sensitivity inversion tests in this study.** Details of the processes and settings are
 163 presented in Fig. S1 and Table 2.

164 2.2.1 Modifying prior emission estimates

165 The prior provides the sectoral profile for subsequent emission attribution. We conducted a comprehensive
 166 examination of associated parameters when updating the prior from 2019 MEIC ($0.5^\circ \times 0.625^\circ$), including
 167 NO_x EFs influencing the conversion of NO_x to CO_2 emissions by sector, threshold value defining the
 168 dominant sector for each grid, and sector classification. For NO_x EFs settings, we devised a ten-level gradient
 169 ranging from -10% to -1% (referred to as ef_ $[-10\%, -1\%]$). Regarding the threshold value, we varied it from
 170 50% to 40% and 60% (referred to as thre_40% and thre_60%), respectively. For sector classification, the
 171 original prior NO_x and CO_2 emissions were updated based on eight sectors in the bottom-up process: power,
 172 industry, cement, iron, residential, residential-bio, on-road, and off-road. This detailed sectoral structure
 173 facilitates relatively detailed bottom-up estimations with specific sectoral activity levels. These eight sectors
 174 were then aggregated into four categories: power, industry (sum of original industry, cement, and iron),
 175 residential (sum of original residential and residential-bio), and transport (sum of original on-road and off-
 176 road) when allocating TROPOMI-constrained total NO_x emissions into sectors. Here, this sector
 177 consolidation, specifically implemented before the bottom-up estimation (4_sectors), was designed to
 178 evaluate the influence of sector classification on the inversion results.

179 2.2.2 Employing coarser model resolution

180 The model resolution of the GEOS-Chem simulation inherently shapes the localized relationship between
 181 NO_2 TVCDs and NO_x emissions established in the top-down process. Finer resolution is advantageous for
 182 establishing localized connections between air pollutant emissions and atmospheric concentrations, and the
 183 attribution of sectoral emissions. However, excessively fine resolution is not applicable due to the inter-grid

184 transport when employing the mass-balance method (Turner et al., 2012). To explore the impact of resolution
185 on emission estimates, we performed an inversion experiment with simulations at a coarser resolution of
186 $2^\circ \times 2.5^\circ$ (Res_2x2.5).

187 **2.2.3 Changing satellite observational constraints**

188 The TROPOMI NO₂ retrievals serve as a constraint in the top-down NO_x emission estimation. We conducted
189 experiments on the TROPOMI NO₂ retrievals through three distinct approaches. Firstly, we used Extreme
190 Gradient Boosting (XGBoost) to fill the invalid satellite retrievals in v2.4 TROPOMI (Trop_fill) by
191 establishing relationships between TROPOMI NO₂ TVCDs and meteorological variables, as well as GEOS-
192 Chem simulated NO₂ TVCDs (modeled_NO₂ in Eq. 6) (Wei et al., 2022). The meteorological variables were
193 derived from European Centre for Medium-Range Weather Forecasts (ECMWF) ERA5 dataset (Hersbach et
194 al., 2020), including boundary layer height (BLH), surface pressure (SP), temperature (TEM), dewpoint
195 temperature (DT), 10m u-component (WU), 10m v-component of winds (WV), total precipitation (TP),
196 evaporation (EP), downward uv radiation at the surface (surUV), and mean surface downward uv radiation
197 flux (downUV). In the XGBoost process, we trained the relationship for daily NO₂ TVCDs throughout the
198 year grid-by-grid, with 80% of the data used as the training set and 20% as the test set.

$$199 \quad \text{TROPOMI_NO}_2 \sim f_{\text{XGBoost}}(\text{modeled_NO}_2, \text{BLH}, \text{SP}, \text{TEM}, \text{DT}, \text{WU}, \text{WV}, \text{TP}, \text{EP}, \text{surUV}, \text{downUV}) \quad (6)$$

200 The comparison of NO₂ TVCDs before and after data filling revealed minimal impact from the original
201 missing data (Fig. S4). This is attributed to our system's utilization of a ten-day moving average of NO₂
202 TVCDs, which effectively mitigates the influence of missing data at the grid scale.

203 Secondly, we evaluated the impact of different versions of TROPOMI NO₂ retrievals by substituting the v2.4
204 TROPOMI data with the older v2.3 TROPOMI NO₂ columns (Trop_v2.3). Updates in TROPOMI data
205 products generally help address the low bias of NO₂ concentrations, particularly in heavily polluted regions
206 (Lange et al., 2023; Van Geffen et al., 2022). Thirdly, we adjusted the satellite data screening protocols to
207 investigate the uncertainties associated with satellite observations on emission estimates, which involved
208 varying the cloud fraction (CF) limit to 0.3 (Trop_cf03) or 0.5 (Trop_cf05) and modifying the quality flag
209 (QA) limit to 0.6 (Trop_qa06) or 0.7 (Trop_qa07), respectively. CF and QA serve as crucial parameters in
210 screening applicable NO₂ TVCDs, representing primary sources of uncertainty in satellite observations (Van
211 Geffen et al., 2022; Lange et al., 2023).

212 **2.2.4 Tests on inversion system parameters**

213 In previous studies, the reference year for updating emissions for target years was 2019. Here, we modified
214 the reference year to 2021 (2021_base) to assess its impact. The parameter β represents the localized
215 relationship between changes in NO₂ TVCDs and changes in anthropogenic NO_x emissions (Eq. 2),
216 determining the transition from observed changes in NO₂ TVCDs to changes in anthropogenic NO_x emissions

217 in the top-down process. To explore potential nonlinear responses in the estimated results to this parameter,
 218 we devised a ten-level gradient for β , ranging from -20% to 20% (refer to as $\beta_{[-20\%, 20\%]}$).

219 2.3 Evaluation of different configurations' impact

220 The sensitivity analysis of the NO_x and CO₂ emissions estimated by our inversion system has illuminated
 221 potential sources of uncertainty and the magnitude of their impacts. To quantify the influence of sensitivity
 222 tests on emission estimates, we calculated the Relative Change (RC) between emissions estimated under
 223 different tests and the Base inversion, and one standard deviation (1σ) of RC to evaluate the consistency of
 224 their impact across temporal, sectoral, and spatial scales (details seen in Table 3). It is noteworthy that on the
 225 annual national total emission scale (maximization of all three dimensions), the value of 1σ equals 0.0%.

226 **Table 3. Calculation of RC and 1σ across different dimensions.**

Dimension	Equations	Parameters
Temporal	$RC_t = \frac{E_{t,sensi} - E_{t,base}}{E_{t,base}}$ $\sigma_t = \sqrt{\frac{\sum_t^n (RC_t - \overline{RC_t})^2}{n}}$	<ul style="list-style-type: none"> • t represents timescale, denoting year, month, or ten-day window. • $E_{t,sensi}$ and $E_{t,base}$ denote the national total emissions under a specific sensitivity test and Base on corresponding temporal scale t. • RC_t and σ_t indicate the RC and its 1σ of national total emissions across temporal scales. The σ_t equals 0.0% when t is the yearly scale.
Sectoral	$RC_{t,s} = \frac{E_{t,s,sensi} - E_{t,s,base}}{E_{t,s,base}}$ $\sigma_s = \sqrt{\frac{\sum_t^n (RC_s - \overline{RC_s})^2}{n}} \quad (\text{Daily})$	<ul style="list-style-type: none"> • s represents sector source. • $E_{t,s,sensi}$ and $E_{t,s,base}$ refer to national sectoral emissions under sensitivity test and Base on temporal scale t (annual and daily). • $RC_{t,s}$ indicates the RC of national sectoral emissions on a temporal scale t. • σ_s indicates 1σ of RC of national sectoral emissions on a daily scale.
Spatial	$RC_{t,p/r} = \frac{E_{t,p/r,sensi} - E_{t,p/r,base}}{E_{t,p/r,base}}$ $\sigma_p = \sqrt{\frac{\sum_p^m (RC_p - \overline{RC_p})^2}{m}} \quad (\text{Annual})$ $\sigma_r = \sqrt{\frac{\sum_t^n (RC_r - \overline{RC_r})^2}{n}} \quad (\text{Daily})$	<ul style="list-style-type: none"> • p and r represent province and region (i.e., provincial clusters), respectively. • $E_{t,p/r,sensi}$ and $E_{t,p/r,base}$ refer to provincial/regional total emissions under sensitivity test and Base on temporal scale t (annual and daily). • $RC_{t,p/r}$ indicates the RC of provincial/regional total emissions on a temporal scale t. • σ_p indicates 1σ of RC of annual total emissions on the provincial scale. • σ_r indicates 1σ of RC of regional total emissions on a daily scale.

227

228 In this context, a condition where 1σ is below 4.0% is deemed as a consistent impact on emission outcomes
 229 within certain dimensions (the determination of 4.0% seen in Fig. S5). Conversely, when 1σ exceeds or equals
 230 4.0%, it is indicative of an inconsistent impact. For instance, a daily scale σ_t value of 6.2% in the Res_2×2.5
 231 test (Fig. S6) suggests that the model resolution exerts a temporally inconsistent influence on daily emission
 232 estimates, whereas a daily scale $\sigma_t = 0.0\%$ under ef_-10% indicates temporal consistency in its influence.

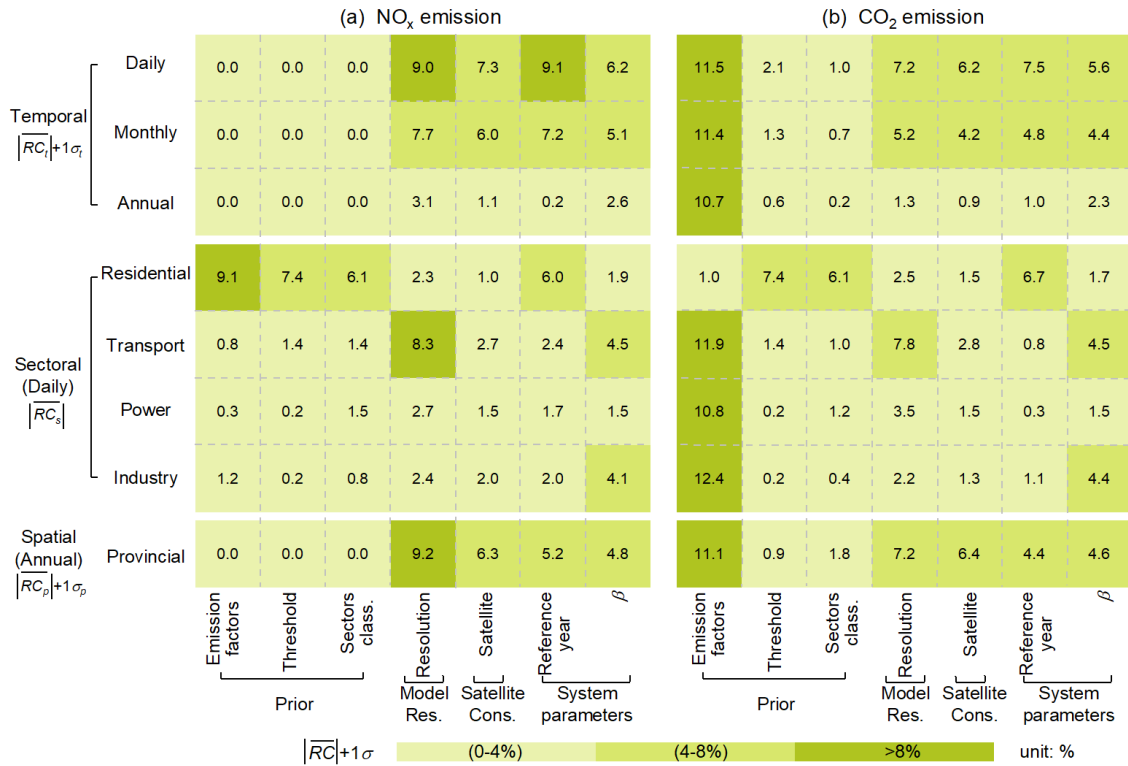
233 These principles extend to other dimensions (i.e., sectoral and spatial). Factors whose sensitivity tests yield
234 large and inconsistent RC across finer time, sector, or region scales tend to introduce high uncertainty and
235 become a priority for future optimization. Conversely, small and consistent RC suggests sources with low
236 uncertainty and a higher level of robustness in the system to those particular factors.

237 3 Results

238 3.1 Overview of the emission responses to sensitivity tests

239 For a comprehensive understanding of emission sensitivity across various dimensions, we compute the sum
240 of absolute average RC and 1σ (i.e., $|\overline{RC}|+1\sigma$) to delineate potential most likely uncertainties associated with
241 tested factors across spatial, temporal, and sectoral scales (Fig. 2). The impact of these tests on emissions are
242 comparable between NO_x and CO_2 , except for the NO_x EFs tests (first column in Fig. 2), which distinctly
243 influence NO_x and CO_2 emissions. CO_2 emissions display high sensitivity to NO_x EFs across all dimensions
244 compared to NO_x emissions, except in the residential sector where NO_x emissions are more responsive while
245 CO_2 emissions are not. For instance, ef_{-10%} (maximum reduction in NO_x EFs tests) incurs a $|\overline{RC}|+1\sigma$ of
246 10.7% in annual national CO_2 emissions, with no corresponding impact on NO_x emissions. The relationship
247 between annual national CO_2 emissions and NO_x EFs exhibits linearity (Fig. S7), remaining within a 4.0%
248 range if NO_x EFs reductions are kept below 4.0% (i.e., ef_[-4%, -1%]). In contrast, daily residential emissions
249 show a $|\overline{RC}|$ of only 1.0% in CO_2 but up to 9.1% in NO_x emissions under the ef_{-10%} test.

250 The remaining sensitivity tests, excluding the NO_x EFs, demonstrate comparable influences on both NO_x and
251 CO_2 emissions. Among all dimensions examined, the annual national total NO_x and CO_2 emissions emerge
252 as robust results, with a $|\overline{RC}|+1\sigma$ of no more than 4.0% across tests. At a finer temporal scale (i.e., daily
253 basis), the impacts of model resolution, reference year, and satellite constraint on estimated emissions are
254 amplified, with their $|\overline{RC}|+1\sigma$ tripling compared to the annual scale. This amplification primarily arises from
255 the increased 1σ on the daily scale (Fig. S6), indicating the substantial impact of these factors on daily
256 emission estimates. At a finer spatial scale, provincial emissions are vulnerable to changes in model
257 resolution, reference year, and satellite constraint due to their impacts' inconsistency in space (Fig. S6).
258 Concerning sectoral emissions, industry and power sector emissions exhibit robustness, whereas transport
259 and residential emissions present vulnerabilities to model resolution and dominant sector threshold value,
260 respectively. In the following sections, we elaborate on the impacts of all sensitivity tests on NO_x and CO_2
261 emissions from temporal, sectoral, and spatial perspectives. To clarify the RC across different dimensions,
262 we adopt RC_t , RC_s , and $RC_{p/r}$ to signify RC in temporal, sectoral, and spatial contexts, respectively.



263

264 **Figure 2. An overview of sensitivity inversion tests' impacts on (a) NO_x and (b) CO₂ emissions.** The
 265 color blocks in this figure represent the sum of absolute average RC and 1σ (i.e., $|\overline{RC}|+1\sigma$), which reflect
 266 the extent of the corresponding tests' impact. Sectoral and provincial results are depicted on an annual scale.
 267 The numbers within each grid represent the maximum value of $|\overline{RC}|+1\sigma$ under tests on corresponding factors.
 268 For example, the $|\overline{RC}|+1\sigma$ noted in the Emission factors column refers to ef_{-10%}. It is noteworthy that the
 269 sectoral dimensions in this figure display their absolute average RC on the daily scale, with their
 270 corresponding 1σ shown separately in Fig. S6.

271 3.2 Emission sensitivity at different temporal scales

272 To exclusively examine emission sensitivities in the temporal dimension, this section focuses on the variation
 273 of national total emissions in each test. Tests influencing both NO_x and CO₂ emissions exhibit comparable
 274 effects, while prior tests exclusively influence CO₂ emissions (Fig. 3). For conciseness, we focus on the RC_t
 275 in CO₂ emissions in tests here (discussion on NO_x emissions seen in Text S3). The average RC_t of national
 276 total emissions are comparable across temporal scales with differences below 1% (lines in Fig. 3, Figs. S8-
 277 S9). However, the consistency of RC_t weakens from yearly to monthly to daily scales (increased $1\sigma_t$ as shown
 278 by the shadow in Fig. 3). To better characterize the extent of the tests' impact, the discussion here focuses on
 279 the $\overline{RC}_t \pm 1\sigma_t$ on a daily scale, reflecting the magnitude and consistency of the impact concurrently.

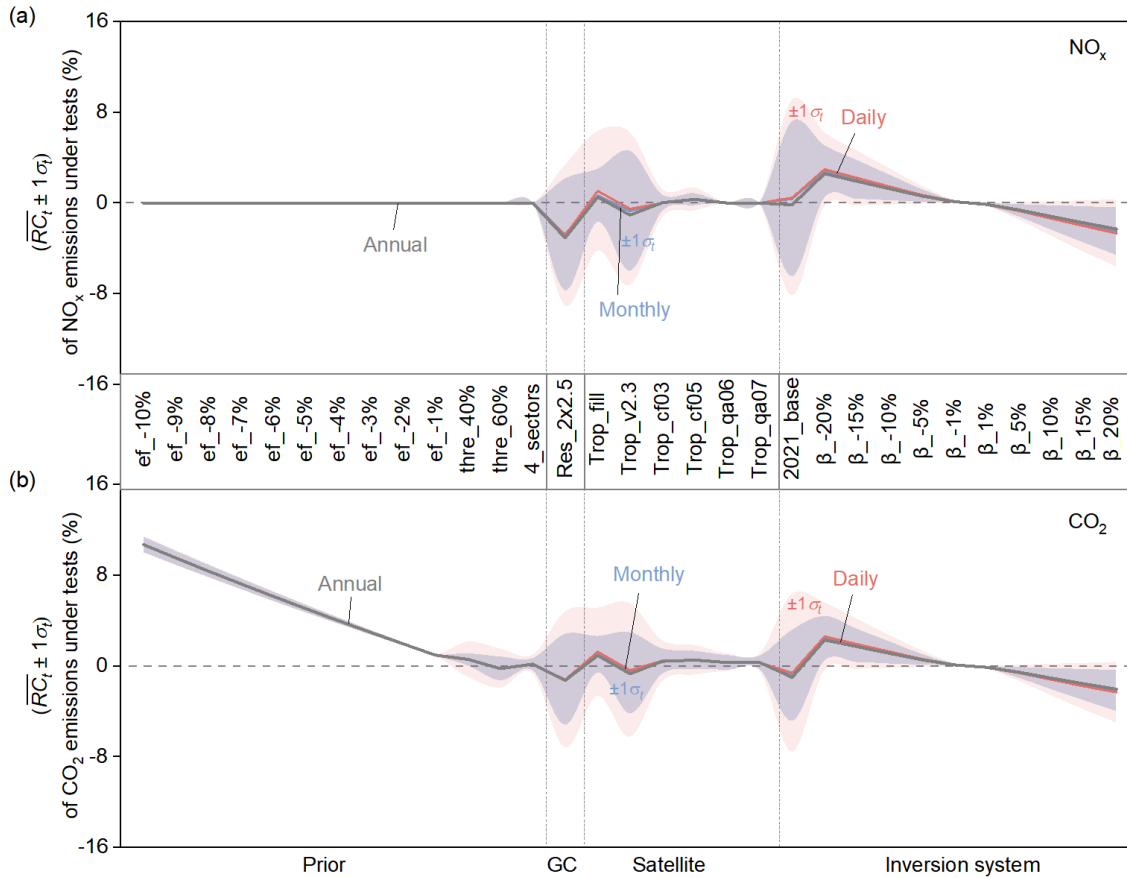
280 At the national total scale, prior tests (ef_[-10%, -1%], thre_{40%/60%}, and 4 sectors) influence CO₂
 281 emissions consistently over time while leaving NO_x emissions unaffected (Fig. 3). This occurs because these
 282 tests only impact sectoral attribution and CO₂-to-NO_x emission ratios. Total NO_x emissions are determined
 283 in the top-down process before sectoral attribution, thus remaining unchanged (Fig. S1). However, sector-

284 specific CO₂ emissions, derived from NO_x emissions, are influenced due to the varying CO₂-to-NO_x emission
285 ratios among sectors (Fig. S10). A reduction in NO_x EFs increases r_{NO_x} , thereby increasing the sectoral CO₂-
286 to-NO_x emission ratios since CO₂ EFs are assumed to be unchanged (Eq. 5). This results in a linear elevation
287 of CO₂ emissions in tandem with the decreased NO_x EFs (Fig. S7), with CO₂ emission variations reaching
288 up to 10.7%±0.7% under $ef_{-10\%}$. Similarly, modifications in threshold values and sector classification alter
289 the identification of dominant sectors per grid, changing the sectoral attribution. Thre_40%/60% and
290 4_sectors bring about $\overline{RC}_t \pm 1\sigma_t$ of 0.6%±1.5%, -0.2%±1.7%, and 0.2%±0.8% in CO₂ emissions, respectively,
291 demonstrating their low influence on emission estimates. Despite differences in the magnitude of prior tests'
292 impacts (\overline{RC}_t), they share a consistency at finer temporal scales, with daily $1\sigma_t$ below 4.0%.

293 Changes in model resolution (Res_2×2.5) introduce the largest variation in estimates among all sensitivity
294 tests, triggering $\overline{RC}_t \pm 1\sigma_t$ of -1.2%±6.0% in daily CO₂ emissions. Its notable inconsistency of impact on the
295 finer temporal scale ($1\sigma_t > 4.0\%$) can be traced back to its induced spatiotemporally diverse changes in β
296 (Figs. S11a and S11b). The overall low estimate of β under Res_2×2.5 results in negative RC_t , and the uneven
297 spatial distribution of β explains the large $1\sigma_t$.

298 As for the impact of satellite constraint, the systematic changes such as missing value supplementation
299 (Trop_fill) or version changes (Trop_v2.3) have a larger impact with daily CO₂ emission variations of
300 1.3%±3.9% and -0.4%±5.9%, while alterations in satellite data quality screening conditions
301 (Trop_cf/Trop_qa) exert a relatively minor impact on estimates with $\overline{RC}_t \pm 1\sigma_t$ less than 0.5%±1.8%. The
302 spatiotemporal changes in satellite NO₂ retrievals contribute to the inconsistent effects of Trop_fill and
303 Trop_v2.3 on daily emissions. However, the small $1\sigma_t$ in screening condition tests suggests that the
304 uncertainty of satellite retrievals has a minor impact on estimates unless there are systematic changes,
305 possibly because we used the ten-day moving average of satellite observation data to constrain emissions.

306 Among inversion system parameter tests, the alteration of the reference year (2021_base) exhibits a notable
307 temporally inconsistent impact, with $\overline{RC}_t \pm 1\sigma_t$ of -0.6%±6.9% in daily CO₂ emissions. This inconsistency
308 can be attributed to the spatiotemporally diverse changes in β , similar to the model resolution test (Figs. S11c
309 and S11d). In contrast, changes in β ($\beta_{[-20\%, 20\%]}$) exert a more notable but consistent impact on estimates,
310 linearly strengthening as the tested amplitude increases (Fig. S7), with $\beta_{20\%}$ triggering variations of
311 2.6%±3.0% in CO₂ emissions. The spatiotemporally uniform changes in β act linearly on the inversion
312 estimate of NO_x emissions (Eq. 1), and then on CO₂ emissions. Therefore, their impact remains consistent on
313 a daily scale.



314

315 **Figure 3. Comparison of the impacts of various tests on national total (a) NO_x and (b) CO₂ emissions**
 316 **at different time scales.** Gray lines correspond to the RC_t in annual emissions. Blue lines depict the average
 317 RC_t in monthly emissions, with the blue shadow indicating monthly scale $1\sigma_t$. Red lines illustrate the average
 318 RC_t in daily emissions, accompanied by the red shadow indicating daily scale $1\sigma_t$.

319 **3.3 Emission sensitivity across source sectors**

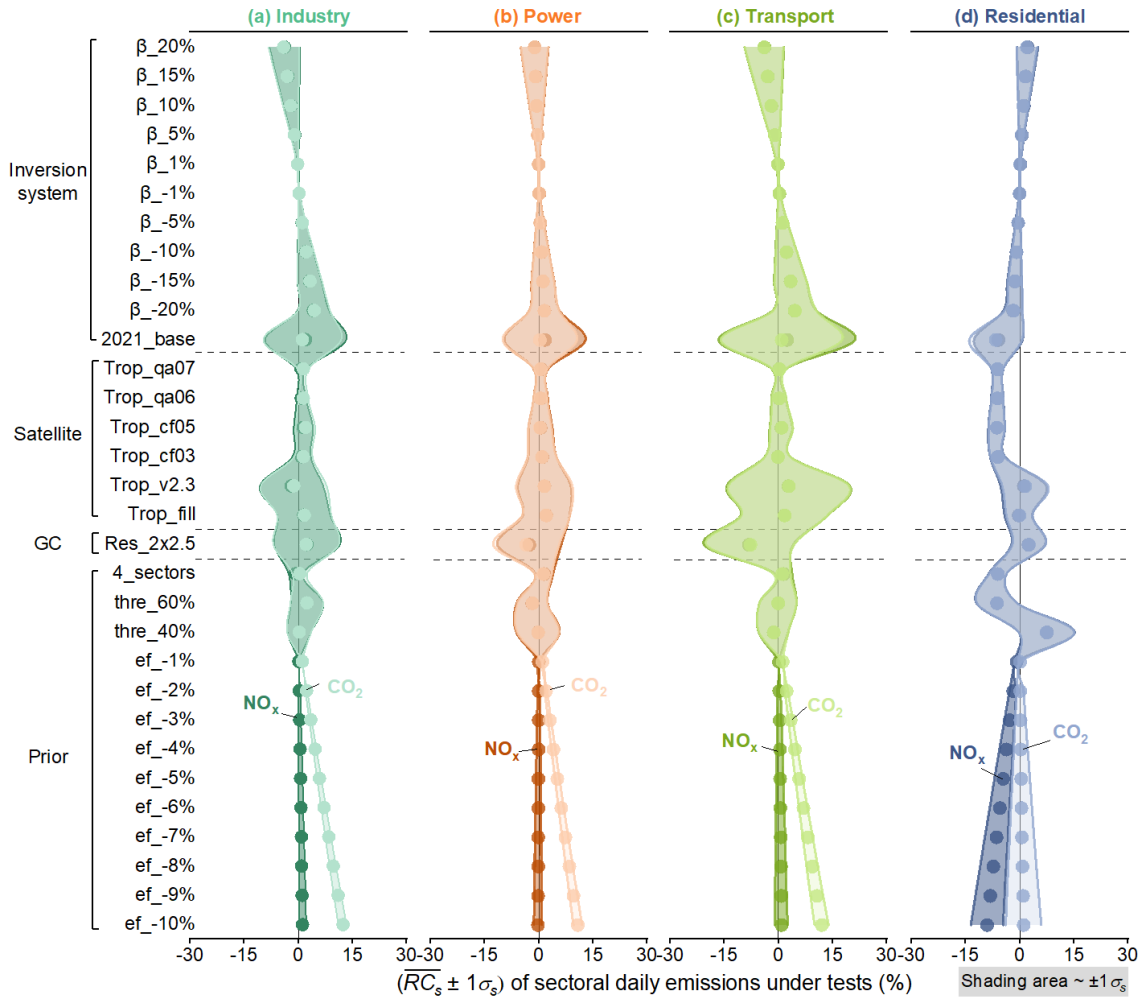
320 Regarding daily national sectoral NO_x and CO₂ emissions, their responses to different sensitivity tests, in
 321 terms of both emission magnitude and consistency ($\overline{RC_s} \pm 1\sigma_s$), are largely similar, except for NO_x EFs tests
 322 (ef_ $[-10\%, -1\%]$) (Fig. 4). Therefore, we primarily discuss the impacts of tests on sectoral emissions using
 323 CO₂ as a representative (refer to Text S4 for discussion on sectoral NO_x emission), and then delve into
 324 elucidating the divergent impact of NO_x EFs on sectoral NO_x and CO₂ emissions.

325 Irrespective of NO_x emission factor changes (ef_ $[-10\%, -1\%]$), industrial and power emissions exhibit greater
 326 robustness than transport and residential emissions, which are more susceptible to different configurations.
 327 Specifically, residential emissions demonstrate the highest susceptibility to reference year, showing
 328 $\overline{RC_s} \pm 1\sigma_s$ of up to $-6.7\% \pm 7.3\%$ in CO₂ emissions in 2021_base test, and exclusively display notable
 329 sensitivity to prior tests (4_sectors and thre_40%/60%) compared to other sectors (Fig. 4). In contrast,
 330 transport emissions are notably influenced by model resolution, with Res_2x2.5 incurring CO₂ emission
 331 variations of $-7.8\% \pm 12.2\%$. Among all sensitivity tests, the model resolution stands out as the most influential

332 factor on sectoral emissions, because the resolution of grid cells affects the determination of the dominant
333 source sector.

334 The overall largest sensitivity of residential emissions to sensitivity tests is potentially attributed to its low
335 proportion to total emissions (Fig. S12). Take $thre_{40\%/60\%}$ as an example, lowering the threshold from 50%
336 to 40% results in identifying more grids as residential source dominant. This, in turn, leads to an increase in
337 residential emission proportions when allocating the total TROPOMI-constrained NO_x emissions into sectors
338 and subsequently CO_2 emissions. Conversely, fewer grids are assigned as residential-dominant when the
339 threshold rises from 50% to 60%, resulting in lower residential emissions (Fig. S13). The next sensitive sector
340 is transport, particularly vulnerable to model resolution, which may be associated with its characteristics in
341 spatial distribution. Transport-dominant grids, particularly those with truck emissions, are typically located
342 close to industry-dominant grids whose NO_x emissions outweigh those from the transport (Zheng et al., 2020).
343 The use of a coarser horizontal resolution could result in a diminished attribution of emissions to transport
344 (Fig. S14).

345 The reduction in NO_x EFs ($ef_{[-10\%, -1\%]}$) is the only test impacting sectoral NO_x and CO_2 emissions
346 differently. For NO_x emissions, the residential sector shows the strongest sensitivity with $\overline{RC_s} \pm 1\sigma_s$ of up to
347 $-9.1\% \pm 4.5\%$ under $ef_{-10\%}$. However, its influence on CO_2 emissions is most pronounced in all sectors
348 except residential, with variations of $12.4\% \pm 1.1\%$ in CO_2 emissions from industry, $11.9\% \pm 1.9\%$ from
349 transport, $10.8\% \pm 1.2\%$ from power, but only $1.0\% \pm 4.9\%$ from residential sectors under $ef_{-10\%}$. The
350 reduction in NO_x EFs shifts the dominant sector attribution, substantially lowering NO_x emissions from the
351 residential sector due to its vulnerability to these changes, similar to the impact seen with the $thre_{60\%}$. The
352 other sectoral (industry, transport, and power) CO_2 emissions present stronger sensitivity to NO_x EFs tests,
353 linearly correlated with the extent of EFs changes. The decline in sectoral NO_x EFs linearly reduces rNO_x
354 (Eq. 5), raising the corresponding CO_2 emissions by increasing sectoral CO_2 -to- NO_x emission ratios.



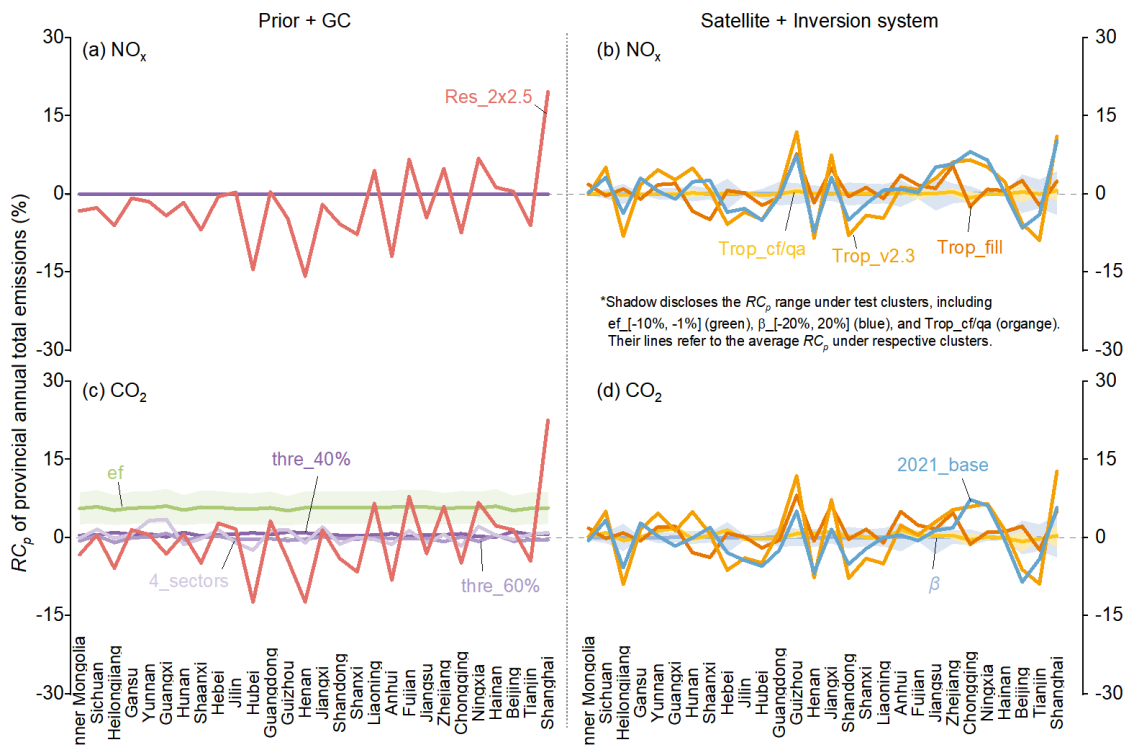
355

356 **Figure 4. Response of sectoral national NO_x and CO₂ emissions to different sensitivity tests on a daily**
 357 **scale.** From left to right, the panels correspond to the (a) industry, (b) power, (c) transport, and (d) residential
 358 source sectors, as the label notes. The dots inside each figure are the average RC_s of daily NO_x (deep color)
 359 and CO₂ (light color) emissions incurred by corresponding tests. The shading area indicates the $1\sigma_s$ of
 360 daily sectoral emissions in different tests.

361 3.4 Emission sensitivity at subnational scales

362 Refining spatial coverage from national to subnational level (i.e., province) reveals that factors causing
 363 inconsistent impacts over finer time scales also tend to induce inconsistent impacts on more granular spatial
 364 regions (Fig. 5). On the annual total scales, the RC_p of NO_x and CO₂ emissions at the provincial scale closely
 365 resemble each other under most sensitivity tests, except for prior tests that only influence CO₂ emissions (Fig.
 366 S15). When comparing across provinces, the sensitivity of emissions to tests correlates with the size of the
 367 provincial area, with smaller regions exhibiting greater susceptibility. Shanghai, the smallest provincial-level
 368 administrative unit in China in terms of area, experiences the largest RC_p throughout China in nearly all tests.
 369 Conversely, Inner Mongolia, one of China's top three largest provinces, undergoes the minimum RC_p in all
 370 tests. Under Res_2×2.5, the RC_p of annual total NO_x and CO₂ emissions in Shanghai are 19.6% and 22.6%,
 371 respectively, while in Inner Mongolia, they are -3.2% and -3.3%. Employing a resolution of 2°×2.5° in

372 Shanghai is impractical in real-world applications, as it would result in fewer than two grids covering the
 373 area. Henan also encounters substantial RC_p under Res_2x2.5, reaching as high as -15.8% and -12.4% in
 374 annual total NO_x and CO_2 emissions. This could be attributed to its proximity to Shandong, a province with
 375 approximately twice the emissions of Henan, making Henan particularly sensitive to the changes in model
 376 resolution due to the overlapping grid cells. It is noteworthy that Guizhou exhibits the highest sensitivity to
 377 satellite constraint, with RC_p reaching up to 11.9% and 11.8% in annual total NO_x and CO_2 emissions under
 378 Trop_v2.3. This sensitivity is attributed to the high cloudiness of the Yunnan-Guizhou Plateau, causing
 379 satellite observations to be highly uncertain over Guizhou (Wang et al., 2023; Li et al., 2021; Cai et al., 2022).

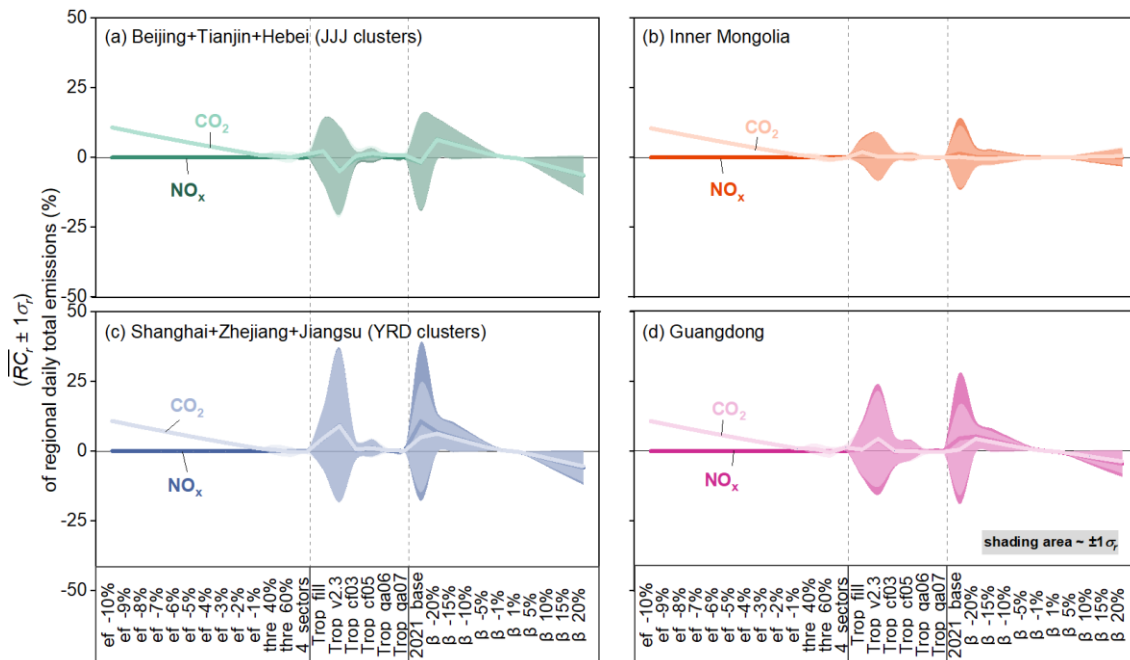


380

381 **Figure 5. Response of provincial annual total NO_x and CO_2 emissions to different tests.** (a) and (b) show
 382 RC_p of NO_x emissions incurred by tests. (c) and (d) are plotted for CO_2 emission as (a) and (b). Lines refer
 383 to the RC_p caused by the corresponding test or the averaged RC_p caused by corresponding test clusters (ef_[-
 384 10%, -1%] and β [-20%, 20%]), and the shadow refers to the RC_p range in test clusters. Only provinces with
 385 enough TROPOMI observations are shown here (i.e., grids with NO_2 TVCDs larger than 1×10^{15}
 386 molecules/cm² cover more than 90% of anthropogenic NO_x emissions within provinces). The provinces are
 387 arranged by area.

388 To further investigate the daily total emission response ($\overline{RC_r} \pm 1\sigma_r$) to tests at the regional scale, we select
 389 and analyze Jing-Jin-Ji clusters (JJJ, including Beijing, Tianjin, and Hebei), Inner Mongolia, Yangtze River
 390 Delta clusters (YRD, including Shanghai, Zhejiang, and Jiangsu), and Guangdong (the location of the Pearl
 391 River Delta). These regions respectively represent an industrialized region with high population density, an
 392 industrialized region with sparse population density, and two major economic development zones with high
 393 population density in China (Fig. 6). Geographically, these regions span North China (JJJ and Inner
 394 Mongolia), East China (YRD), and South China (Guangdong), thereby covering different meteorological and

395 geographic factors. Overall, the $\overline{RC_r} \pm 1\sigma_r$ of daily regional emissions are similar for NO_x and CO₂ except for
 396 ef_[-10%, -1%], resembling their daily national emission responses (Fig. 3). The $\overline{RC_r} \pm 1\sigma_r$ of daily regional
 397 emissions is especially notable in YRD and Guangdong (southern part of China). This could be attributed to
 398 the relatively low NO₂ concentration in southern China (Fig. S4), making them particularly sensitive to spatial
 399 variations in parameters, such as the β in 2021_base (Fig. S11) and NO₂ TVCDs in Trop_v2.3 test. Besides,
 400 the cloud fraction is higher in southern China, introducing larger uncertainties in remote sensing (Liu et al.,
 401 2019; Latsch et al., 2022). The emission responses to prior and β _[-20%, 20%] tests are close for these four
 402 regions, particularly in the prior tests, suggesting that these impacts on emissions are less dependent on
 403 geographic factors.



404
 405 **Figure 6. Response of regional total NO_x and CO₂ emissions to tests on a daily scale.** (a), (b), (c), and (d)
 406 show the $\overline{RC_r} \pm 1\sigma_r$ of daily NO_x (deep color) and CO₂ (light color) emissions in different tests in Jing-Jin-Ji
 407 clusters (Beijing, Tianjin, and Hebei), Inner Mongolia, Yangtze River Delta clusters (Shanghai, Zhejiang,
 408 and Jiangsu), and Guangdong. The shading area inside each figure refers to the corresponding 1 σ_r . It is worth
 409 noting that the Res_{2×2.5} test is not shown here since the resolution of 2°×2.5° proves too coarse for certain
 410 regions, rendering it unrealistic for real-world applications. The result containing Res_{2×2.5} is present in SI
 411 as Fig. S16 for reference.

412 4 Discussion

413 This study delineates an approximate spectrum of uncertainties inherent in deriving conclusions of varying
 414 precision with our air pollution satellite sensor-based CO₂ emission inversion system. When interpreting
 415 conclusions based on the emission data derived from such an inversion system, it is practical and imperative
 416 to aggregate emissions across different dimensions to fulfill specific usage requirements. Direct utilization
 417 of data with all fine-grained resolutions at temporal, sectoral, and spatial dimensions poses challenges. If

418 adhering to a variation tolerance of 5%, the reliability of annual national NO_x and CO₂ emissions is
419 established in most cases. Notably, careful attention is needed when selecting model resolution and attributing
420 sectoral emissions. Expanding the tolerance to 10%, which is still below the conventional bottom-up method's
421 uncertainty range of 13%-37% (Zhao et al., 2011; Huo et al., 2022), renders annual regional or daily national
422 emissions robust from an average perspective. Nevertheless, meticulous scrutiny is advised when drawing
423 conclusions based on daily sectoral or daily regional emissions, especially in specific regions (e.g., Shanghai,
424 Guizhou). The large uncertainty of daily sectoral emission is typically observed in other emission datasets,
425 such as Carbon Monitor (up to 40% uncertainty) (Liu et al., 2020c; Huo et al., 2022). Further liberalizing the
426 tolerance to 25%, which is quite uncertain for scientific and policy-making purposes, the majority of
427 conclusions derived from our estimates stand as reliable. The extensive tolerance range primarily stems from
428 regional emissions, posing a challenging issue for many emission inversion techniques. For example, the
429 uncertainty in NO_x emissions derived from the 2D MISATEAM (chemical transport Model-Independent
430 SATellite-derived Emission estimation Algorithm for Mixed-sources) method is approximately 20% for large
431 and mid-size US cities (Liu et al., 2023), and the uncertainty for daily NO_x and CO₂ emissions based on the
432 superposition model ranges from 37% to 48% on a city scale (Zhang et al., 2023). Notably, remarkable
433 advancements have been achieved in estimating subnational CO₂ emissions through CO₂-observing satellites,
434 such as sectoral CO₂ assessments with OCO-3 (Roten et al., 2023), and urban emission optimizations utilizing
435 the Orbiting Carbon Observatory-2 (OCO-2) (Yang et al., 2020; Ye et al., 2020). Yet, reducing uncertainties
436 at subnational scales remains an ongoing challenge.

437 This study paves the way for the continuous improvement of the current air pollution satellite sensor-based
438 CO₂ emission inversion system. Firstly, prioritizing a nimble and appropriate horizontal resolution is crucial
439 for establishing accurate localized relationships between NO₂ TVCDs and NO_x emissions, contributing to
440 improved NO_x and CO₂ emission estimations from temporal, sectoral, and spatial perspectives. Secondly, the
441 more accurate satellite observation is conducive to reducing the uncertainty in final results, presenting
442 increasing promise with advancements in remote sensing technology. Besides, the progress in multi-species
443 synchronous observations through satellite and aircraft platforms offers alternative verification for multi-
444 species emission inversion, such as the Copernicus Anthropogenic Carbon Dioxide Monitoring constellation
445 (CO2M) (Sierk et al., 2021). Thirdly, the reliability of sectoral NO_x EFs changes, which determine CO₂-to-
446 NO_x emission ratios, is essential for the accurate conversion from NO_x to CO₂ emissions. This underscores
447 the need to acquire more accurate NO_x EFs. While obtaining on-site measurements of CO₂-to-NO_x emission
448 ratios is challenging, efforts are underway to enhance its configuration. An iterative modification of NO_x EFs
449 within the current system could be incorporated, minimizing the gap between bottom-up updated and
450 TROPOMI-constrained sectoral NO_x emissions to below 2%. This approach yields more accurate CO₂-to-
451 NO_x emission ratios and CO₂ emissions (Fig. S17). The optimized CO₂ emission change from 2021 to 2022
452 is +0.6%, reflecting a more precise representation of the growth in fossil fuel consumption (+1.9%). Fourthly,
453 utilizing a more refined approach to determine dominant sectors at a grid level can reduce the uncertainty of
454 small-contributing sectoral emissions, particularly in the residential sector. These enhancements will improve

455 the system's accuracy in estimating emissions across all dimensions, positioning it as a valuable tool for
456 simultaneous inversion-based monitoring of greenhouse gas and air pollutants emissions, ultimately
457 supporting a strategic roadmap for the vision of clean air and climate warming mitigation.

458

459 *Code and data availability.* The source code of the GEOS-Chem model is available at
460 <https://geoschem.github.io/>. The prior NO_x and CO₂ emissions of 2019 MEIC (v1.4) are available at
461 http://meicmodel.org.cn/?page_id=541&lang=en. The v2.4.0 TROPOMI NO₂ column concentrations are
462 publicly available at https://www.temis.nl/airpollution/no2col/no2regio_tropomi.php. The activity level data
463 of China from 2019 to 2022 including the industrial production of cement, iron, thermal electricity, etc., are
464 available at <https://data.stats.gov.cn/english/easyquery.htm?cn=C01>.

465 *Supplement.* The supplement related to this article is available online.

466 *Author Contributions.* Bo Zheng designed the research and led the analysis. Hui Li performed the simulation,
467 analyzed the data, and created the graphs. Bo Zheng, Jiabin Qiu, and Hui Li wrote the manuscript.

468 *Competing interests.* The authors declare that they have no conflict of interest.

469 *Acknowledgements.* The authors thank the editor and the anonymous referees for helpful comments that have
470 improved the paper.

471 *Financial support.* This work was supported by the National Key R&D Program of China (2023YFC3705601)
472 and National Natural Science Foundation of China (Grant No. 42375096).

473 **References**

- 474 Cai, D., Tao, L., Yang, X.-Q., Sang, X., Fang, J., Sun, X., Wang, W., and Yan, H.: A climate
475 perspective of the quasi-stationary front in southwestern China: structure, variation and impact,
476 *Climate Dynamics*, 59, 547-560, [10.1007/s00382-022-06151-1](https://doi.org/10.1007/s00382-022-06151-1), 2022.
- 477 Cheng, J., Tong, D., Liu, Y., Bo, Y., Zheng, B., Geng, G., He, K., and Zhang, Q.: Air quality and
478 health benefits of China's current and upcoming clean air policies, *Faraday Discussions*, 226,
479 584-606, <https://doi.org/10.1039/D0FD00090F>, 2021.
- 480 Cooper, M., Martin, R. V., Padmanabhan, A., and Henze, D. K.: Comparing mass balance and
481 adjoint methods for inverse modeling of nitrogen dioxide columns for global nitrogen oxide
482 emissions, *Journal of Geophysical Research: Atmospheres*, 122, 4718-4734,
483 [10.1002/2016JD025985](https://doi.org/10.1002/2016JD025985), 2017.
- 484 Cooper, M. J., Martin, R. V., Hammer, M. S., Levelt, P. F., Veefkind, P., Lamsal, L. N., Krotkov, N.
485 A., Brook, J. R., and McLinden, C. A.: Global fine-scale changes in ambient NO₂ during COVID-19
486 lockdowns, *Nature*, 601, 380-387, <https://doi.org/10.1038/s41586-021-04229-0>, 2022.
- 487 Goldberg, D. L., Lu, Z., Oda, T., Lamsal, L. N., Liu, F., Griffin, D., McLinden, C. A., Krotkov, N. A.,
488 Duncan, B. N., and Streets, D. G.: Exploiting OMI NO₂ satellite observations to infer fossil-fuel
489 CO₂ emissions from U.S. megacities, *Science of The Total Environment*, 695, 133805,
490 [10.1016/j.scitotenv.2019.133805](https://doi.org/10.1016/j.scitotenv.2019.133805), 2019.
- 491 Guevara, M., Petetin, H., Jorba, O., Denier van der Gon, H., Kuenen, J., Super, I., Granier, C.,
492 Doumbia, T., Ciais, P., Liu, Z., Lamboll, R. D., Schindlbacher, S., Matthews, B., and Pérez García-
493 Pando, C.: Towards near-real-time air pollutant and greenhouse gas emissions: lessons learned
494 from multiple estimates during the COVID-19 pandemic, *Atmospheric Chemistry and Physics*, 23,
495 8081-8101, <https://doi.org/10.5194/acp-23-8081-2023>, 2023.
- 496 Hersbach, H., Bell, B., Berrisford, P., Hirahara, S., and Thépaut, J.: The ERA5 global reanalysis,
497 *Quarterly Journal of the Royal Meteorological Society*, 2020.
- 498 Huo, D., Liu, K., Liu, J., Huang, Y., Sun, T., Sun, Y., Si, C., Liu, J., Huang, X., Qiu, J., Wang, H., Cui, D.,
499 Zhu, B., Deng, Z., Ke, P., Shan, Y., Boucher, O., Darnet, G., Liang, G., Zhao, J., Chen, L., Zhang, Q.,
500 Ciais, P., Zhou, W., and Liu, Z.: Near-real-time daily estimates of fossil fuel CO₂ emissions from
501 major high-emission cities in China, *Sci Data*, 9, 684, [10.1038/s41597-022-01796-3](https://doi.org/10.1038/s41597-022-01796-3), 2022.
- 502 Ke, P., Deng, Z., Zhu, B., Zheng, B., Wang, Y., Boucher, O., Arous, S. B., Zhou, C., Andrew, R. M.,
503 Dou, X., Sun, T., Song, X., Li, Z., Yan, F., Cui, D., Hu, Y., Huo, D., Chang, J.-P., Engelen, R., Davis, S.
504 J., Ciais, P., and Liu, Z.: Carbon Monitor Europe near-real-time daily CO₂ emissions for 27 EU
505 countries and the United Kingdom, *Scientific Data*, 10, 374, [10.1038/s41597-023-02284-y](https://doi.org/10.1038/s41597-023-02284-y), 2023.
- 506 Lamsal, L. N., Martin, R. V., Padmanabhan, A., van Donkelaar, A., Zhang, Q., Sioris, C. E., Chance,
507 K., Kurosu, T. P., and Newchurch, M. J.: Application of satellite observations for timely updates
508 to global anthropogenic NO_x emission inventories, *Geophysical Research Letters*, 38,
509 <https://doi.org/10.1029/2010gl046476>, 2011.
- 510 Lange, K., Richter, A., Schönhardt, A., Meier, A. C., Bösch, T., Seyler, A., Krause, K., Behrens, L. K.,
511 Wittrock, F., Merlaud, A., Tack, F., Fayt, C., Friedrich, M. M., Dimitropoulou, E., Van Roozendaal,
512 M., Kumar, V., Donner, S., Dörner, S., Lauster, B., Razi, M., Borger, C., Uhlmannsiek, K., Wagner,
513 T., Ruhtz, T., Eskes, H., Bohn, B., Santana Diaz, D., Abuhassan, N., Schüttemeyer, D., and
514 Burrows, J. P.: Validation of Sentinel-5P TROPOMI tropospheric NO₂ products by comparison
515 with NO₂ measurements from airborne imaging DOAS, ground-based stationary DOAS, and
516 mobile car DOAS measurements during the S5P-VAL-DE-Ruhr campaign, *Atmos. Meas. Tech.*, 16,
517 1357-1389, <https://doi.org/10.5194/amt-16-1357-2023>, 2023.
- 518 Latsch, M., Richter, A., Eskes, H., Sneep, M., Wang, P., Veefkind, P., Lutz, R., Loyola, D., Argyrouli,
519 A., Valks, P., Wagner, T., Sihler, H., van Roozendaal, M., Theys, N., Yu, H., Siddans, R., and

520 Burrows, J. P.: Intercomparison of Sentinel-5P TROPOMI cloud products for tropospheric trace
521 gas retrievals, *Atmos. Meas. Tech.*, 15, 6257-6283, 10.5194/amt-15-6257-2022, 2022.

522 Le Quéré, C., Peters, G. P., Friedlingstein, P., Andrew, R. M., Canadell, J. G., Davis, S. J., Jackson,
523 R. B., and Jones, M. W.: Fossil CO₂ emissions in the post-COVID-19 era, *Nature Climate Change*,
524 11, 197-199, <https://doi.org/10.1038/s41558-021-01001-0>, 2021.

525 Li, H. and Zheng, B.: Toward monitoring daily anthropogenic CO₂ emissions with air pollution
526 sensors from space, *One Earth*, 7, 1846-1857, 10.1016/j.oneear.2024.08.019, 2024.

527 Li, H., Zheng, B., Ciais, P., Boersma, K. F., Riess, T. C. V. W., Martin, R. V., Broquet, G., van der A,
528 R., Li, H., Hong, C., Lei, Y., Kong, Y., Zhang, Q., and He, K.: Satellite reveals a steep decline in
529 China's CO₂ emissions in early 2022, *Science Advances*, 9, eadg7429,
530 <https://doi.org/10.1126/sciadv.adg7429>, 2023.

531 Li, J., Sun, Z., Liu, Y., You, Q., Chen, G., and Bao, Q.: Top-of-Atmosphere Radiation Budget and
532 Cloud Radiative Effects Over the Tibetan Plateau and Adjacent Monsoon Regions From CMIP6
533 Simulations, *Journal of Geophysical Research: Atmospheres*, 126, e2020JD034345,
534 10.1029/2020JD034345, 2021.

535 Li, L., Zhang, Y., Zhou, T., Wang, K., Wang, C., Wang, T., Yuan, L., An, K., Zhou, C., and Lu, G.:
536 Mitigation of China's carbon neutrality to global warming, *Nat Commun*, 13, 5315,
537 10.1038/s41467-022-33047-9, 2022.

538 Liu, F., Duncan, B. N., Krotkov, N. A., Lamsal, L. N., Beirle, S., Griffin, D., McLinden, C. A.,
539 Goldberg, D. L., and Lu, Z.: A methodology to constrain carbon dioxide emissions from coal-fired
540 power plants using satellite observations of co-emitted nitrogen dioxide, *Atmos. Chem. Phys.*,
541 20, 99-116, <https://doi.org/10.5194/acp-20-99-2020>, 2020a.

542 Liu, F., Beirle, S., Joiner, J., Choi, S., Tao, Z., Knowland, K. E., Smith, S. J., Tong, D. Q., Ma, S.,
543 Fasnacht, Z. T., and Wagner, T.: High-resolution Mapping of Nitrogen Oxide Emissions in Large
544 US Cities from TROPOMI Retrievals of Tropospheric Nitrogen Dioxide Columns, *EGU sphere*,
545 2023, 1-18, 10.5194/egusphere-2023-1842, 2023.

546 Liu, F., Page, A., Strode, S. A., Yoshida, Y., Choi, S., Zheng, B., Lamsal, L. N., Li, C., Krotkov, N. A.,
547 Eskes, H., van der A, R., Veeckind, P., Levelt, P. F., Hauser, O. P., and Joiner, J.: Abrupt decline in
548 tropospheric nitrogen dioxide over China after the outbreak of COVID-19, *Science Advances*, 6,
549 eabc2992, <https://doi.org/10.1126/sciadv.abc2992>, 2020b.

550 Liu, Y., Tang, Y., Hua, S., Luo, R., and Zhu, Q.: Features of the Cloud Base Height and Determining
551 the Threshold of Relative Humidity over Southeast China, *Remote Sensing*, 11, 2900, 2019.

552 Liu, Z., Ciais, P., Deng, Z., Lei, R., Davis, S. J., Feng, S., Zheng, B., Cui, D., Dou, X., Zhu, B., Guo, R.,
553 Ke, P., Sun, T., Lu, C., He, P., Wang, Y., Yue, X., Wang, Y., Lei, Y., Zhou, H., Cai, Z., Wu, Y., Guo, R.,
554 Han, T., Xue, J., Boucher, O., Boucher, E., Chevallier, F., Tanaka, K., Wei, Y., Zhong, H., Kang, C.,
555 Zhang, N., Chen, B., Xi, F., Liu, M., Bréon, F.-M., Lu, Y., Zhang, Q., Guan, D., Gong, P., Kammen, D.
556 M., He, K., and Schellnhuber, H. J.: Near-real-time monitoring of global CO₂ emissions reveals the
557 effects of the COVID-19 pandemic, *Nature Communications*, 11, 5172,
558 <https://doi.org/10.1038/s41467-020-18922-7>, 2020c.

559 MacDonald, C. G., Mastrogiacomo, J. P., Laughner, J. L., Hedelius, J. K., Nassar, R., and Wunch,
560 D.: Estimating enhancement ratios of nitrogen dioxide, carbon monoxide and carbon dioxide
561 using satellite observations, *Atmos. Chem. Phys.*, 23, 3493-3516, <https://doi.org/10.5194/acp-23-3493-2023>, 2023.

563 Martin, R. V., Jacob, D. J., Chance, K., Kurosu, T. P., Palmer, P. I., and Evans, M. J.: Global
564 inventory of nitrogen oxide emissions constrained by space-based observations of NO₂ columns,
565 *Journal of Geophysical Research: Atmospheres*, 108, <https://doi.org/10.1029/2003JD003453>,
566 2003.

567 Meinshausen, M., Lewis, J., McGlade, C., Gutschow, J., Nicholls, Z., Burdon, R., Cozzi, L., and
568 Hackmann, B.: Realization of Paris Agreement pledges may limit warming just below 2 degrees
569 C, *Nature*, 604, 304-309, <https://doi.org/10.1038/s41586-022-04553-z>, 2022.

570 Miyazaki, K. and Bowman, K.: Predictability of fossil fuel CO₂ from air quality emissions, *Nature*
571 *Communications*, 14, 1604, <https://doi.org/10.1038/s41467-023-37264-8>, 2023.

572 Mun, J., Choi, Y., Jeon, W., Lee, H. W., Kim, C.-H., Park, S.-Y., Bak, J., Jung, J., Oh, I., Park, J., and
573 Kim, D.: Assessing mass balance-based inverse modeling methods via a pseudo-observation test
574 to constrain NO_x emissions over South Korea, *Atmospheric Environment*, 292, 119429,
575 <https://doi.org/10.1016/j.atmosenv.2022.119429>, 2023.

576 Nassar, R., Hill, T. G., McLinden, C. A., Wunch, D., Jones, D. B. A., and Crisp, D.: Quantifying CO₂
577 Emissions From Individual Power Plants From Space, *Geophysical Research Letters*, 44, 10,045-
578 010,053, 10.1002/2017GL074702, 2017.

579 Reuter, M., Buchwitz, M., Schneising, O., Krautwurst, S., O'Dell, C. W., Richter, A., Bovensmann,
580 H., and Burrows, J. P.: Towards monitoring localized CO₂ emissions from space: co-located
581 regional CO₂ and NO₂ enhancements observed by the OCO-2 and S5P satellites, *Atmos. Chem.*
582 *Phys.*, 19, 9371-9383, <https://doi.org/10.5194/acp-19-9371-2019>, 2019.

583 Roten, D., Lin, J. C., Das, S., and Kort, E. A.: Constraining Sector-Specific CO₂ Fluxes Using Space-
584 Based XCO₂ Observations Over the Los Angeles Basin, *Geophysical Research Letters*, 50,
585 e2023GL104376, <https://doi.org/10.1029/2023GL104376>, 2023.

586 Shan, Y., Ou, J., Wang, D., Zeng, Z., Zhang, S., Guan, D., and Hubacek, K.: Impacts of COVID-19
587 and fiscal stimuli on global emissions and the Paris Agreement, *Nature Climate Change*, 11, 200-
588 206, <https://doi.org/10.1038/s41558-020-00977-5>, 2021.

589 Sierk, B., Fernandez, V., Bézy, J.-L., Meijer, Y., Durand, Y., Bazalgette Courrèges-Lacoste, G.,
590 Pachot, C., Löscher, A., Nett, H., Minoglou, K., Boucher, L., Windpassinger, R., Pasquet, A., Serre,
591 D., and te Hennepe, F.: The Copernicus CO₂M mission for monitoring anthropogenic carbon
592 dioxide emissions from space, *International Conference on Space Optics — ICSO 2021, SPIE2021*.

593 Taylor, T. E., O'Dell, C. W., Baker, D., Bruegge, C., Chang, A., Chapsky, L., Chatterjee, A., Cheng,
594 C., Chevallier, F., Crisp, D., Dang, L., Drouin, B., Eldering, A., Feng, L., Fisher, B., Fu, D., Gunson,
595 M., Haemmerle, V., Keller, G. R., Kiel, M., Kuai, L., Kurosu, T., Lambert, A., Laughner, J., Lee, R.,
596 Liu, J., Mandrake, L., Marchetti, Y., McGarragh, G., Merrelli, A., Nelson, R. R., Osterman, G.,
597 Oyafuso, F., Palmer, P. I., Payne, V. H., Rosenberg, R., Somkuti, P., Spiers, G., To, C., Weir, B.,
598 Wennberg, P. O., Yu, S., and Zong, J.: Evaluating the consistency between OCO-2 and OCO-3
599 XCO₂ estimates derived from the NASA ACOS version 10 retrieval algorithm, *Atmos. Meas. Tech.*,
600 16, 3173-3209, 10.5194/amt-16-3173-2023, 2023.

601 Turner, A. J., Henze, D. K., Martin, R. V., and Hakami, A.: The spatial extent of source influences
602 on modeled column concentrations of short-lived species, *Geophysical Research Letters*, 39,
603 <https://doi.org/10.1029/2012GL051832>, 2012.

604 van Geffen, J., Eskes, H., Compernolle, S., Pinardi, G., Verhoelst, T., Lambert, J. C., Sneep, M., ter
605 Linden, M., Ludewig, A., Boersma, K. F., and Veefkind, J. P.: Sentinel-5P TROPOMI NO₂ retrieval:
606 impact of version v2.2 improvements and comparisons with OMI and ground-based data,
607 *Atmos. Meas. Tech.*, 15, 2037-2060, <https://doi.org/10.5194/amt-15-2037-2022>, 2022.

608 Wang, Z., Zhang, M., Li, H., Wang, L., Gong, W., and Ma, Y.: Bias correction and variability
609 attribution analysis of surface solar radiation from MERRA-2 reanalysis, *Climate Dynamics*,
610 10.1007/s00382-023-06873-w, 2023.

611 Wei, J., Liu, S., Li, Z., Liu, C., Qin, K., Liu, X., Pinker, R. T., Dickerson, R. R., Lin, J., Boersma, K. F.,
612 Sun, L., Li, R., Xue, W., Cui, Y., Zhang, C., and Wang, J.: Ground-Level NO₂ Surveillance from Space
613 Across China for High Resolution Using Interpretable Spatiotemporally Weighted Artificial
614 Intelligence, *Environ Sci Technol*, 56, 9988-9998, 10.1021/acs.est.2c03834, 2022.

615 Wren, S. N., McLinden, C. A., Griffin, D., Li, S.-M., Cober, S. G., Darlington, A., Hayden, K., Mihele,
616 C., Mittermeier, R. L., Wheeler, M. J., Wolde, M., and Liggio, J.: Aircraft and satellite
617 observations reveal historical gap between top-down and bottom-up CO₂ emissions from
618 Canadian oil sands, *PNAS Nexus*, 2, <https://doi.org/10.1093/pnasnexus/pgad140>, 2023.
619 Yang, E. G., Kort, E. A., Ott, L. E., Oda, T., and Lin, J. C.: Using Space-Based CO₂ and NO₂
620 Observations to Estimate Urban CO₂ Emissions, *Journal of Geophysical Research: Atmospheres*,
621 128, e2022JD037736, <https://doi.org/10.1029/2022JD037736>, 2023.
622 Yang, E. G., Kort, E. A., Wu, D., Lin, J. C., Oda, T., Ye, X., and Lauvaux, T.: Using Space-Based
623 Observations and Lagrangian Modeling to Evaluate Urban Carbon Dioxide Emissions in the
624 Middle East, *Journal of Geophysical Research: Atmospheres*, 125, e2019JD031922,
625 <https://doi.org/10.1029/2019JD031922>, 2020.
626 Ye, C., Zhou, X., Pu, D., Stutz, J., Festa, J., Spolaor, M., Tsai, C., Cantrell, C., Mauldin, R. L.,
627 Campos, T., Weinheimer, A., Hornbrook, R. S., Apel, E. C., Guenther, A., Kaser, L., Yuan, B., Karl,
628 T., Haggerty, J., Hall, S., Ullmann, K., Smith, J. N., Ortega, J., and Knote, C.: Rapid cycling of
629 reactive nitrogen in the marine boundary layer, *Nature*, 532, 489-491, 10.1038/nature17195,
630 2016.
631 Ye, X., Lauvaux, T., Kort, E. A., Oda, T., Feng, S., Lin, J. C., Yang, E. G., and Wu, D.: Constraining
632 Fossil Fuel CO₂ Emissions From Urban Area Using OCO-2 Observations of Total Column CO₂,
633 *Journal of Geophysical Research: Atmospheres*, 125, e2019JD030528,
634 <https://doi.org/10.1029/2019JD030528>, 2020.
635 Zhang, Q., Boersma, K. F., Zhao, B., Eskes, H., Chen, C., Zheng, H., and Zhang, X.: Quantifying
636 daily NO_x and CO₂ emissions from Wuhan using satellite observations from TROPOMI and OCO-
637 2, *Atmos. Chem. Phys.*, 23, 551-563, 10.5194/acp-23-551-2023, 2023.
638 Zhang, Q., Zheng, Y., Tong, D., Shao, M., Wang, S., Zhang, Y., Xu, X., Wang, J., He, H., Liu, W.,
639 Ding, Y., Lei, Y., Li, J., Wang, Z., Zhang, X., Wang, Y., Cheng, J., Liu, Y., Shi, Q., Yan, L., Geng, G.,
640 Hong, C., Li, M., Liu, F., Zheng, B., Cao, J., Ding, A., Gao, J., Fu, Q., Huo, J., Liu, B., Liu, Z., Yang, F.,
641 He, K., and Hao, J.: Drivers of improved PM_{2.5} air quality in China from 2013 to 2017, *Proc Natl*
642 *Acad Sci USA*, 116, 24463-24469, 10.1073/pnas.1907956116, 2019.
643 Zhao, Y., Nielsen, C. P., Lei, Y., McElroy, M. B., and Hao, J.: Quantifying the uncertainties of a
644 bottom-up emission inventory of anthropogenic atmospheric pollutants in China, *Atmos. Chem.*
645 *Phys.*, 11, 2295-2308, 10.5194/acp-11-2295-2011, 2011.
646 Zheng, B., Geng, G., Ciais, P., Davis, S. J., Martin, R. V., Meng, J., Wu, N., Chevallier, F., Broquet,
647 G., Boersma, F., van der A, R., Lin, J., Guan, D., Lei, Y., He, K., and Zhang, Q.: Satellite-based
648 estimates of decline and rebound in China's CO₂ emissions during COVID-19 pandemic, *Science*
649 *Advances*, 6, eabd4998, <https://doi.org/10.1126/sciadv.abd4998>, 2020.
650 Zheng, B., Tong, D., Li, M., Liu, F., Hong, C., Geng, G., Li, H., Li, X., Peng, L., Qi, J., Yan, L., Zhang,
651 Y., Zhao, H., Zheng, Y., He, K., and Zhang, Q.: Trends in China's anthropogenic emissions since
652 2010 as the consequence of clean air actions, *Atmos. Chem. Phys.*, 18, 14095-14111,
653 10.5194/acp-18-14095-2018, 2018.

654